The Effects of Surface Heterogeneity Scale on the Flux Imbalance

YanzhaoZhou[1, 2], Dan Li[3], and Xin Li[4, 5]

[1]Key Laboratory of Remote Sensing of Gansu Province, Northwest Institute of Eco-Environment and Resources, Chinese Academy of Sciences, Lanzhou, 730000, Gansu, China.

[2]University of Chinese Academy of Sciences, Beijing, 100101, China.

[3]Department of Earth and Environment, Boston University, Boston, 02215, Massachusetts, USA.

[4] Institute of Tibetan Plateau Research, Chinese Academy of Sciences, Beijing, 100101, China.

[5]CAS Center for Excellence in Tibetan Plateau Earth Sciences, Chinese Academy of Sciences, Beijing, 100101, China.

Corresponding author: Xin Li (lixin@lzb.ac.cn) and Dan Li (lidan@bu.edu)

Key Points:

- The ratio of boundary-layer height to the Obukhov length (z_i/L), the integral length scale of vertical velocity (l_w), the mean horizontal velocity (U), and the average interval (T) control the flux imbalance (I);
- Based on LES results, a diagnostic equation for the flux imbalance is proposed as $I = 1-[az/z_i + b][-K \times z_i/L \times l_w/UT + C]$, where a, b, K, and C are empirical constants and b should in theory equal to unity.
- Compared to the other models, this model is derived from the cospectrum and hence is more physically based. Moreover, the relations between the flux imbalance and various factors reported in the literature can be explained by this model.

Abstract It is well known that the available energy (i.e., the net radiation minus the ground heat flux) is often 10% ~ 30% larger than the sum of turbulent fluxes measured by the eddy-covariance method. Although field observations and previous large-eddy simulation (LES) studies have shown that surface heterogeneity can induce flux imbalance, the relationship between the flux imbalance magnitude and the surface heterogeneity scale remains underexplored. In this paper, we examine the flux imbalance over landscapes characterized by different surface heterogeneity scales in a dry convective boundary layer. Results show that the flux imbalance initially increases with increasing surface heterogeneity scale, reaches its peak value when the surface heterogeneity scale is on the order of the convective boundary-layer height (z_i), and then slightly decreases. Based on LES results, we propose a conceptual model to explain how flux imbalance is influenced by surface heterogeneity. We argue that the ratio of boundary-layer height to the Obukhov length (z_i/L), the integral length scale of vertical velocity (l_w), the mean horizontal velocity (U), and the average interval (T) control the flux imbalance. Among these four variables, l_w determines the size of turbulent coherent structures (i.e., large eddies); whereas z_i/L affects the form of these large eddies. Meanwhile, the U and T determine the number of these large eddies that can be sampled by the eddy-covariance sensors in a finite averaging period. This finding indicates that it may be possible to diagnose the flux imbalance using these four variables.

Keywords Convective boundary layer • Flux imbalance • Large eddy simulation • Surface heterogeneity scale

1 Introduction

The eddy-covariance (EC) method is one of the most common methods for measuring turbulent exchanges between the biosphere and the atmosphere. The fluxes of heat, water vapor and CO_2 measured at EC sites around the world (e.g., FLUXNET) are widely used for developing and validating land surface schemes in climate models (Williams et al., 2009), and for climatological studies (Jung et al., 2010). However, a long-standing problem with the EC method is observed in which, the sum of the sensible and latent heat fluxes by EC is smaller than the difference between the net radiation and ground heat flux (Aubinet et al., 2012; Foken, 2008; Leuning et al. 2012; Oncley et al., 2007; Twine et al., 2000; Wilson et al., 2002; Xu et al., 2017). This systematic bias in the EC method is called the surface energy imbalance or non-closure problem and has been one of the biggest challenges for using EC measurements.

Potential reasons for this energy imbalance include mismatch in the footprints of radiation and turbulent flux measurements, measurement/computation errors, significant advective fluxes, and inadequate sampling of large-scale, low-frequency turbulent eddies, as reviewed elsewhere (Mahrt, 1998; Twine et al., 2000; Foken et al, 2006; Foken, 2008; Wang et al., 2009; Foken et al., 2011; Leuning et al. 2012; Wohlfahrt and Widmoser, 2013). Among these potential causes, the inadequate sampling of large-scale turbulent eddies has been increasingly acknowledged as one of the leading contributors to the surface energy imbalance (Foken et al., 2011).

Over homogeneous terrain, the largest turbulent eddy scales with the boundary-layer height (Wyngaard, 1985; Stull, 1988). Over heterogeneous terrain, secondary circulations can be further induced by the landscape-level heterogeneity around EC sites (Foken et al, 2006). These large-scale turbulent eddies and secondary circulations may not be adequately sampled by an EC tower in a finite averaging period (e.g., 30 mins); hence, an imbalance occurs. This phenomenon has been confirmed by many observational (Panin et al., 1998; Stoy et al., 2013; Eder et al., 2015a; Gao et al., 2017; Xu et al., 2017) and large-eddy simulation (LES) studies (Kanda et al., 2004; Inagaki et al., 2006; Steinfeld et al., 2007; Huang et al., 2008; Eder et al., 2015b; Schalkwijk et al., 2016; De Roo and Mauder, 2018; Zhou et al., 2018).

Over the past decade, the understanding of flux imbalance has been significantly advanced and many factors were found to be related to the flux imbalance (see Table 1). However, it remains elusive as to (i) how the flux imbalance is influenced by surface heterogeneity and (ii) what the relationship between the flux imbalance magnitude and the surface heterogeneity scale is. For example, although previous studies have shown that surface heterogeneity is a major factor causing flux imbalance (Zhou et al., 2018) and various energy balance closure parametrization schemes have been proposed (Panin et al., 1998; Huang et al., 2008; Panin and Bernhofer, 2008), the key flow and surface variables controlling the flux imbalance magnitude remain debated (Eder et al., 2014). In addition, while field observations (Stoy et al., 2013; Xu et al., 2017) have shown that the flux imbalance magnitude generally increases as the surface heterogeneity becomes stronger, large variations occur in such relations. Addressing these two questions frames the scope of our study.

The paper is structured as follows: Section 2 describes the method; Section 3 provides details on the LES model and the numerical experiments. The results are described in Section 4 and discussed in Section 5. Finally, Section 6 concludes the paper.

Table 1 A summary of factors affecting the flux imbalance (*I*)

Fators	Relations to *I*	References
Averaging time (*T*)	The smaller *T*, the larger *I*	Finnigan et al. (2003); Charuchittipan et al. (2014); Kanda et al. (2004); Chen et al. (2006); Steinfeld et al. (2007); Schalkwijk et al. (2016); Zhou et al. (2018)
Height (*z*)	The larger *z*, the larger *I*	Kanda et al. (2004); Chen et al. (2006); Steinfeld et al. (2007); Huang et al (2008); Schalkwijk et al. (2016); Zhou et al. (2018)
Horizontal mean velocity (*U*)	The smaller *U*, the larger *I*	Lee (1998); Stoy et al. (2013); Li et al. (2005); Franssen et al. (2010); Kanda et al. (2004); Chen et al. (2006); Steinfeld et al. (2007); Huang et al. (2008); Schalkwijk et al. (2016); Zhou et al. (2018)
The phase difference	The larger the phase difference between ground heat flux and net radiation, the larger *I*; The larger the phase difference between vertical velocity and the scalar, the larger *I*	Gao et al. (2010); Gao et al. (2017)
Surface heterogeneity	The stronger surface heterogeneity, the larger *I*	Panin et al. (1998); Stoy et al. (2013); Xu et al. (2017); Zhou et al. (2018); Inagaki et al. (2006)
u_*/w_*	The smaller u_*/w_*, the larger *I*	Huang et al. (2008); Zhou et al. (2018)
z_i/L	The larger $-z_i/L$, the larger *I*	Schalkwijk et al. (2016)
z/L	The larger $-z/L$, the larger *I*	Franssen et al. (2010); McGloin et al. (2018)
Turbulent intensity	The smaller turbulent intensity, the larger *I*; the smaller turbulent kinetic energy, the larger *I*	Zuo et al. (2012); Zhou et al. (2018)

2 Method

2.1 Flux imbalance over heterogeneous surfaces

We consider a variable φ with the spatial mean as $[\varphi]$ and the temporal mean as $\overline{\varphi}$. Fluctuations from the spatial and temporal means are denoted as φ'' and φ', respectively. The flux imbalance magnitude (*I*) is defined as the difference between "true flux" and the turbulent flux, which can be expressed as follows:

$$I = \frac{TF - TU}{TF}, \quad (1)$$

where *TU* denotes the turbulent flux measured by the EC and *TF* represents the "true flux". Note that here *I* represents the flux imbalance magnitude as *TU* is often smaller than *TF*. This is slightly different from the flux imbalance defined in previous studies (Kanda et al., 2004; Inagaki et al., 2006; Steinfeld et al., 2007; Huang et al., 2008; Schalkwijk et al., 2016; Zhou et al., 2018), which is often (–*I*).

In Finnigan et al. (2003), the authors introduced the assumptions and limitations of the EC method using a control volume approach. In this method, the surface heat flux is treated as the "true flux". The spatiotemporally averaged budget equation for the potential temperature over the cubic control volume can be expressed as follows:

$$\left[\overline{HFX}\right] = \left[\overline{w'\theta'}\right] + \sum_{1}^{4}\left[\overline{v'\theta'}\right] + \left[\overline{w}\overline{\theta}\right] + \sum_{1}^{4}\left[\overline{v}\overline{\theta}\right] + \left[\int \frac{\partial\overline{\theta}}{\partial t} dz\right], \quad (2)$$

where *HFX* denotes the surface heat flux ("true flux"); w and θ indicate the vertical velocity and potential temperature, respectively; *v* represents the velocity vector perpendicular to the lateral faces and $\overline{w'\theta'}$ represents the temporally-averaged vertical turbulent heat flux as measured by the EC method at a single location. Clearly, the other terms on the right-hand side of Eq. (2) denote the items causing the flux imbalance: the horizontal flux divergence, the vertical mean advection, the horizontal mean advection, and the storage of θ within the control volume. In this study, we do not separate the horizontal flux divergence and the vertical and horizontal mean advection terms. The sum of these three terms (the horizontal flux divergence and the vertical and horizontal mean advection) is referred to as the "advection" term in this study. The fraction of "advection" term to the true flux is referred to as the "advection fraction".

The domain averaged flux imbalance magnitude over homogeneous surfaces can thus be calculated as follows:

$$[I] = \left[\frac{\left[\overline{HFX}\right] - \overline{w'\theta'}}{\left[\overline{HFX}\right]}\right], \quad (3)$$

where $[I]$ represents the "mean" difference between the temporal flux (i.e., the flux calculated from the EC method) and the true flux. It should be pointed out that in some previous studies (Kanda et al., 2004; Inagaki et al., 2006; Steinfeld et al., 2007; Huang et al., 2008; Schalkwijk et al., 2016; Zhou et al., 2018), the spatiotemporally averaged vertical heat flux ($\left[\overline{w\theta}\right]$) at a given height is used as the "true flux". This method is often used over homogeneous surfaces (Kanda et al., 2004; Steinfeld et al., 2007; Huang et al., 2008; Schalkwijk et al., 2016; Zhou et al., 2018) and 1-D heterogeneous surfaces (Inagaki et al., 2006; Zhou et al., 2018). In this study, however, we use the surface flux as the true flux.

2.2 The surface heterogeneity scale

Many previous LES studies focused on idealized heterogeneity, such as striped-like and chessboard-like heterogeneities with uniform sizes (Chen and Avissar, 1994; Avissar and Schmidt, 1998). For these idealized heterogeneity patterns, the characteristic length scale can be relatively easily defined. For example, the width of the strip can be used to indicate the length scale of surface heterogeneity. Recently, more complex and/or realistic landscape patterns based on remote sensing have been used (Albertson et al., 2001; Kustas and Albertson, 2003; Bertoldi et al., 2007; Huang and Margulis, 2009; Liu et al., 2017). To characterize the length scale of surface heterogeneity (L_p) over complex landscape patterns, Bou-Zeid et al., (2007) (hereafter B07) proposed to define L_p as follows:

$$L_p = \int_0^{L_D} \left[1 - \frac{D(r)}{\max(D)}\right] dr, \tag{4}$$

where L_D is the streamwise length of the domain and $D(r)$ is the structure function of the analyzed surface characteristics (e.g., momentum roughness length) with distance r along the streamwise direction. On the other hand, Huang and Margulis (2009) (hereafter HM09) used a normalized exponential variogram model to define the characteristic length scale:

$$L_p = -\frac{\ln\gamma}{3d}, \tag{5}$$

where the d is the distance matrix representing the distance between any two points and γ is the variogram. The details about the two methods can be found in B07 and HM09.

2.3 A cospectral model

In this study, we employ the cospectrum, which describes the distribution of flux among scales, to interpret the flux imbalance. Figure 1a presents a schematic illustrating the cospectrum of heat flux ($F_{w\theta}$), where k is the wavenumber and k_p is the wavenumber at which $F_{w\theta}$ reaches its peak (hereafter the peak wavenumber). Within the confines of the cospectrum, we assume that the EC method can only sample eddies that are larger (smaller) than a critical wavenumber (wavelength), which is referred to as k_{ec} (Fig. 1a). This implicitly assumes that the large eddies are responsible for the flux imbalance, which can be calculated as follows:

$$[I] = 1 - \frac{\int_{k_{ec}}^{\infty} F_{w\theta}(k,z)\,dk}{HFX} = 1 - \frac{\int_0^{\infty} F_{w\theta}(k,z)\,dk \left(1 - \frac{\int_0^{k_{ec}} F_{w\theta}(k,z)\,dk}{\int_0^{\infty} F_{w\theta}(k,z)\,dk}\right)}{HFX}. \quad 6)$$

The above expression can be further simplified as follows,

$$[I] = 1 - f_1 f_2. \tag{7}$$

$$f_1 = \frac{\int_0^{\infty} F_{w\theta}(k,z)\,dk}{HFX}. \tag{8}$$

$$f_2 = 1 - \frac{\int_0^{k_{ec}} F_{w\theta}(k,z)\,dk}{\int_0^{\infty} F_{w\theta}(k,z)\,dk}. \tag{9}$$

In Eq. (7), f_1 is the ratio of the "flux at a certain height" to the surface flux and its deviation from unity represents the effect of storage/advection terms in Eq. (2). The term f_2 represents the role of large eddies in causing flux imbalance at any given height z. From Eq. (7) it can be seen that the flux imbalance magitude increases with decreasing f_1 and decreasing f_2.

Different functional forms have been used for the cospectrum $F_{w\theta}$ (Kaimal and Finnigan, 1994; Massman and Lee, 2002; Lee et al., 2005; Katul et al., 2013). In this paper, we use the cospectrum model of Lee et al. (2005) for illustration purpose, as follows:

$$F_{w\theta}(k) = \frac{A}{k_p\left[1 + m\left(\frac{k}{k_p}\right)^{2\mu}\right]^{\frac{1}{2\mu}\frac{m+1}{m}}}, \tag{10}$$

where A is a normalization parameter, m and μ are the (inertial subrange) slope parameter and broadness parameter, respectively. When m = 3/4, Eq. (10) can produce the -7/3 power law of $F_{w\theta}$ in the inertial subrange (Lumley, 1967; Li and Katul, 2017). When μ = 0.5, Eq. (10) can reproduce the observed cospectrum from the famous Kansas experiment (Kaimal et al., 1976), which is commonly used as the standard in the cospectral correction of EC observations (Moore, 1986). Substituting Eq. (10) into Eq. (6), the f_2 term can be expressed as:

$$f_2 = \frac{\Gamma\left(\frac{1}{2\mu}, \frac{m+1}{2\mu}\left(\frac{k_{ec}}{k_p}\right)^{2\mu}\right)}{\Gamma\left(\frac{1}{2\mu}, 0\right)}, \tag{11}$$

where Γ is the incomplete Gamma function. The detailed derivation of Eq. (11) is presented in Appendix A. Because m and μ are positive and $\Gamma(s, x)$ decreases with increasing x, Eq. (11) indicates that f_2 decreases with increasing k_{ec}/k_p. Similar results as Eq. (11) are obtained using other cospectral models as shown in Appendix B but the relation between f_2 and k_{ec}/k_p strongly depends on the assumed cospectral model. As such, we will not use the exact relation between f_2 and k_{ec}/k_p given by the Lee et al. (2005) model (namely, Eq. 11) in our calculation. Instead, the Eq. (11) is meant to provide a qualitative description of the relation between f_2 and k_{ec}/k_p (i.e., f_2 is expected to decrease with increasing k_{ec}/k_p). In Sect. 4.2, we will first explore the behavior of f_1, which will be calculated from Eq. (8), and then explore the relation between f_2, which will be inferred from (1-[I])/f_1, and k_{ec}/k_p.

Now we detail how k_{ec}/k_p is estimated (or approximated). Based on the sampling theory, the larger the eddy moving velocity (say, represented by u), the more eddies can be sampled by the EC in a finite averaging period (T) and hence the smaller the flux imbalance. Therefore, k_{ec} may be represented by $1/(uT)$. A reasonable estimate for u is the mean horizontal velocity U by invoking the Taylor's hypothesis. However, given the limitation of Taylor's hypothesis in constructing very large-scale structures in turbulent boundary layers (Dennis and Nickels, 2008), we will also examine other velocity scales such as the convective velocity w_*, which is defined as follows:

$$w_* = \left(\frac{g}{\rho} z_i \frac{H}{c_p \theta_0}\right)^{\frac{1}{3}}, \tag{12}$$

where g is the gravitational acceleration, θ_0 is the reference potential temperature, c_p is the specific heat of air, and z_i is the boundary-layer height. In addition, we will consider the friction velocity $u_* = \sqrt{\tau/\rho}$, where τ is the surface drag and ρ is the air density, as well as the square root of turbulent kinetic energy (TKE) ($\bar{e} = \sqrt{TKE} = \sqrt{0.5(\sigma_u^2 + \sigma_v^2 + \sigma_w^2)}$, where σ_u^2, σ_v^2, and σ_w^2 are the variances of the three wind velocity components). Note that w_* and u_* have been used in previous studies to characterize the flux imbalance magnitude (Huang et al., 2008).

In addition to k_{ec}, we also need an estimate of k_p, namely, the peak wavenumber. The peak wavenumber k_p can be related to the inverse of the integral length scale or $1/l$ (Kaimal and Finnigan, 1994), which is an estimate of the size of organized turbulent structures in the turbulent boundary layer. It is defined based on the autocorrelation function R as follows:

$$l = \int_0^\infty R(r)dr, \tag{13}$$

where r is the displacement in space. In this study, l is calculated using the autocorrelation function of vertical velocity (l_w) or potential temperature (l_θ) with an integration until the first zero of $R(r)$ (Lenschow and Stankov, 1986).

In a neutrally stratified atmospheric surface layer over homogenous surfaces, the integrate length scale is on the order of z (Kaimal et al., 1976), yielding that [I] increases with $z/(uT)$. This result is in agreement with previous results showing that the flux imbalance magnitude increases with increasing height in the surface layer, decreasing mean horizontal velocity (when u is represented by the mean horizontal velocity), and shorter averaging period over homogeneous surfaces (Kanda et al., 2004; Steinfeld et al., 2007; Schalkwijk et al., 2016; Zhou et al., 2018). This agreement shows that the result from the cospectral model is reasonable (at least over homogeneous surfaces).

It is pointed out again that the relation between f_2 and k_{ec}/k_p is strongly dependent on the assumed cospectral shape. That is, f_2 is not only a function of k_{ec}/k_p as Eq. (11) alludes to. While $l/(uT)$ might provide a good approximation to k_{ec}/k_p, other factors that can affect the cospectral shape (but not explicitly considered by the Lee et al. (2005) cospectral model) need to be further considered. These factors include surface heterogeneity and atmospheric stability, the latter of which can be indicated by z_i/L, where L is the Obukhov length. We choose z_i/L because previous studies (Lee et al, 2005; Moeng and Sullivan, 1994; Khanna and Brasseur, 1998; Schalkwijk et al., 2016) have found that z_i/L strongly affects large-scale turbulent coherent structures and thus the low wavenumber regime of the cospetra (Kaimal and Finnigan, 1994). For example, when $z_i/|L|$ is larger than about 25, cell structures form with polygonal patterns and no noticeable alignment. When $z_i/|L|$ is larger than 5 and smaller than 25, roll structures formed aligned with the wind (Lee et al, 2005). Moreover, previous studies have also found a correlation between the flux imbalance and z_i/L (Schalkwijk et al., 2016; Huang et al., 2008). Therefore, in this study, we use z_i/L to represent the effects of atmospheric stability on turbulent coherent structures and hence on the flux imbalance.

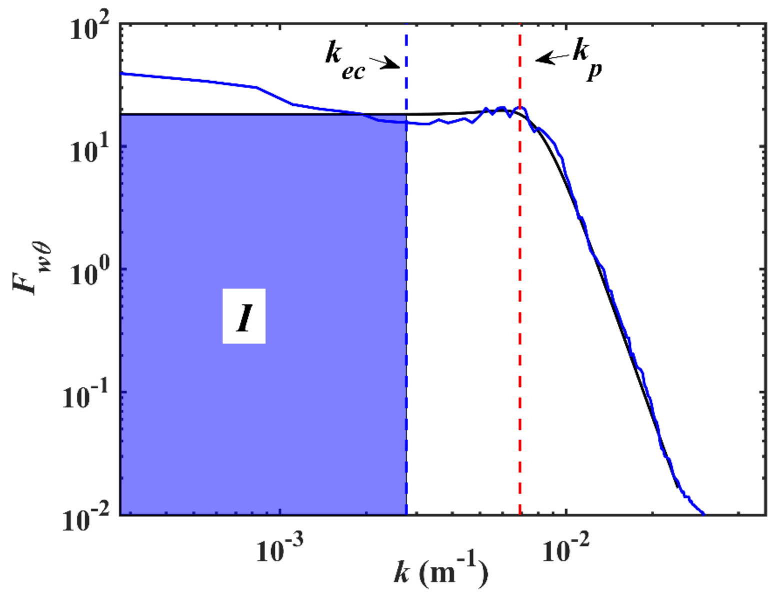

Figure. 1 A conceptual model for flux imbalance from the cospectral perspective. The blue curve is the cospectrum calculated based on the LES results of B2000 (see Sect. 3.2) and the black curve is the fitted cospectrum based on Eq. (10) with k_p=0.007, m=0.18 and μ=5.5. The k is the wavenumber and $F_{w\theta}$ is the cospectrum between w and θ. I is the flux imbalance. The k_p and k_{ec} are the peak wavenumber and critical wavenumber for EC, respectively.

3 Experimental design

3.1 Model description and configuration

It is pointed out again that the relation between f_2 and k_{ec}/k_p is strongly dependent on the assumed cospectral shape. That is, f_2 is not only a function of k_{ec}/k_p as Eq. (11) alludes to. While $l/(uT)$ might provide a good approximation to k_{ec}/k_p, other factors that can affect the cospectral shape (but not explicitly considered by the Lee et al. (2005) cospectral model) need to be further considered. These factors include surface heterogeneity and atmospheric stability, the latter of which can be indicated by z_i/L, where L is the Obukhov length. We choose z_i/L because previous studies (Lee et al, 2005; Moeng and Sullivan, 1994; Khanna and Brasseur, 1998; Schalkwijk et al., 2016) have found that z_i/L strongly affects large-scale turbulent coherent structures and thus the low wavenumber regime of the cospetra (Kaimal and Finnigan, 1994). For example, when $z_i/|L|$ is larger than about 25, cell structures form with polygonal patterns and no noticeable alignment. When $z_i/|L|$ is larger than 5 and smaller than 25, roll structures formed aligned with the wind (Lee et al, 2005). Moreover, previous studies have also found a correlation between the flux imbalance and z_i/L (Schalkwijk et al., 2016; Huang et al., 2008). Therefore, in this study, we use z_i/L to represent the effects of atmospheric stability on turbulent coherent structures and hence on the flux imbalance.

We used the Weather Research and Forecasting (WRF) model version 3.9, which has the LES capability and has been widely used to investigate convective boundary layers over homogeneous and heterogeneous surfaces (Moeng et al., 2007; Patton et al., 2005; Talbot et al., 2012; Zhu et al., 2016). Following Zhu et al., (2016), the original WRF-LES model was modified so that the surface temperature, instead of the surface heat flux, can be prescribed as the surface boundary condition.

Except for the surface layer scheme, other physical schemes in the WRF-LES model such as microphysics and radiation are all turned off. In the surface layer scheme, Monin-Obukhov similarity theory is used to calculate sensible heat flux from the prescribed surface temperature and the simulated air temperature. Periodic boundary conditions are used in our simulations. In addition, we use the default WRF numerical discretization options (i.e., a fifth-order scheme for advection in the horizontal direction, a third-order scheme for advection in the vertical direction and a third-order Runge-Kutta scheme for the time integration). For the subgrid-scale turbulence parameterization, the 1.5-order turbulent kinetic energy-based closure scheme is used. The subgrid-scale flux is added to the turbulent flux.

The simulation domain is 5 km × 5 km × 2 km in the x, y and z directions, respectively, and the number of grid points is 100 × 100 × 100. Hence, the resolution in x- and y- directions is 50 m and ranges from 6 m ~ 20 m in the z-direction (Talbot et al., 2012). The time step is 0.25 s. The model is initialized with an idealized neutral boundary-layer profile, in which the potential temperature is 298 K below 850 m, with a strong inversion layer of a potential temperature surge of 60 K km^{-1} from 850 to 1050 m. The potential temperature gradient is 3 K km^{-1} above 1050 m. All cases had the same initial atmospheric conditions. The geostrophic wind is set to be zero in all cases.

3.2 Numerical Experiments

In this study, we simulate a dry atmosphere over a heterogeneous surface composed of random configurations of patches with different surface temperatures and momentum roughness lengths. We design two cases to analyze the effects of different heterogeneity scales on the flux imbalance. The key information is summarized in Table 2.

Similar to B07, a baseline surface configuration is created manually with relatively large patches (Fig. 2a). Subsequently, the baseline configuration is changed to create surfaces with different heterogeneity length scales. With different methods, two types of simulations are designed. The cases denoted by ‘B’ used the method from B07 (e.g., Eq. 6) and cases denoted by ‘H’ used the method from HM09 (e.g., Eq. 7). Due to the use of the same baseline configuration, the probability density functions (pdfs) of surface properties are identical in the two types of simulations. For each type, four simulations are performed with different heterogeneity length scales (e.g., 2000 m, 1200 m, 550 m and 240 m). These scales are chosen to give a broad range of surface heterogeneity scales: one simulation with a heterogeneity scale larger than the boundary-layer height (2000 m), one simulation with a heterogeneity scale on the order of boundary-layer height (1200 m), and two simulations with heterogeneity scales smaller than the boundary-layer height (550 m and 240 m). The spatial patterns of surface temperature in the above mentioned simulations are shown in Fig. 2. Note that the statistical properties (i.e., the pdfs) in all cases are same.

For all simulations, a 2-hour spin-up is used (Patton et al., 2005). The temporal statistics are calculated for all grid points, i.e., all the grids in the domain are virtual towers.

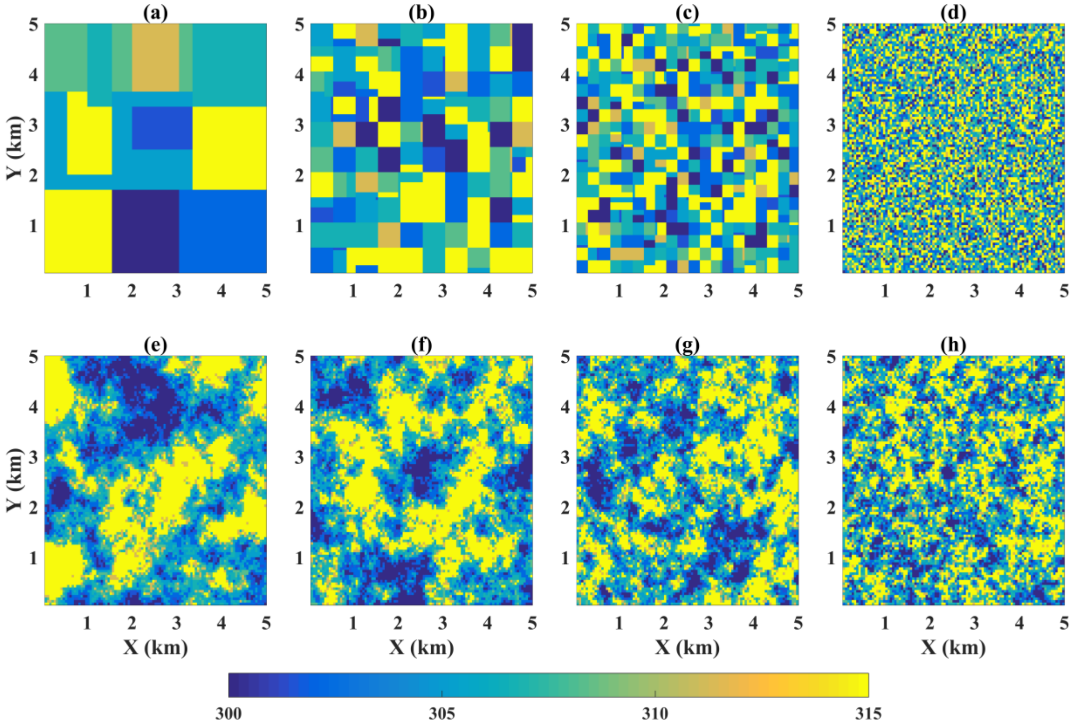

Figure. 2 Spatial patterns of surface temperature in B cases (a to d) and H cases (e to h).

Table 2. Summary of the experiments along with spatially and temporally averaged ABL characteristics in case B and H. The z_i represents the boundary-layer height and the u_* and w_* indicate the friction velocity and convective velocity, respectively.

Case Name	Heterogeneity scales (m)	z_i (m)	u_* (m/s)	w_* (m/s)
B2000	2000	1215	0.37	2.64
B1200	1200	1211	0.36	2.74
B550	550	1168	0.40	2.73
B240	240	1154	0.43	2.62
H2000	2000	1254	0.42	2.91
H1200	1200	1249	0.40	2.90
H550	550	1210	0.43	2.80
H240	240	1228	0.43	2.80

4 Results

4.1 The effects of surface heterogeneity scale on flux imbalance magnitude

4.1.1 The simulated ABL structures

As shown in Fig. 2, the patterns of surface temperature (and roughness length, not shown) are significantly different between B cases and H cases. As a result, the vertical profiles of momentum and scalars under convective conditions are also different, which can be clearly seen from Fig. 3 for B2000 and H2000. The horizontal slice is at 2 m above ground. Clearly, “plumes” can be observed emanating from places where the surface temperature is higher. However, the spatial distributions of these “plumes” are significantly different because of the different spatial configurations of surface temperature. As the heterogeneity scale increases, larger organized structures are formed as shown in Fig. 4, which is similar to the results of HM09.

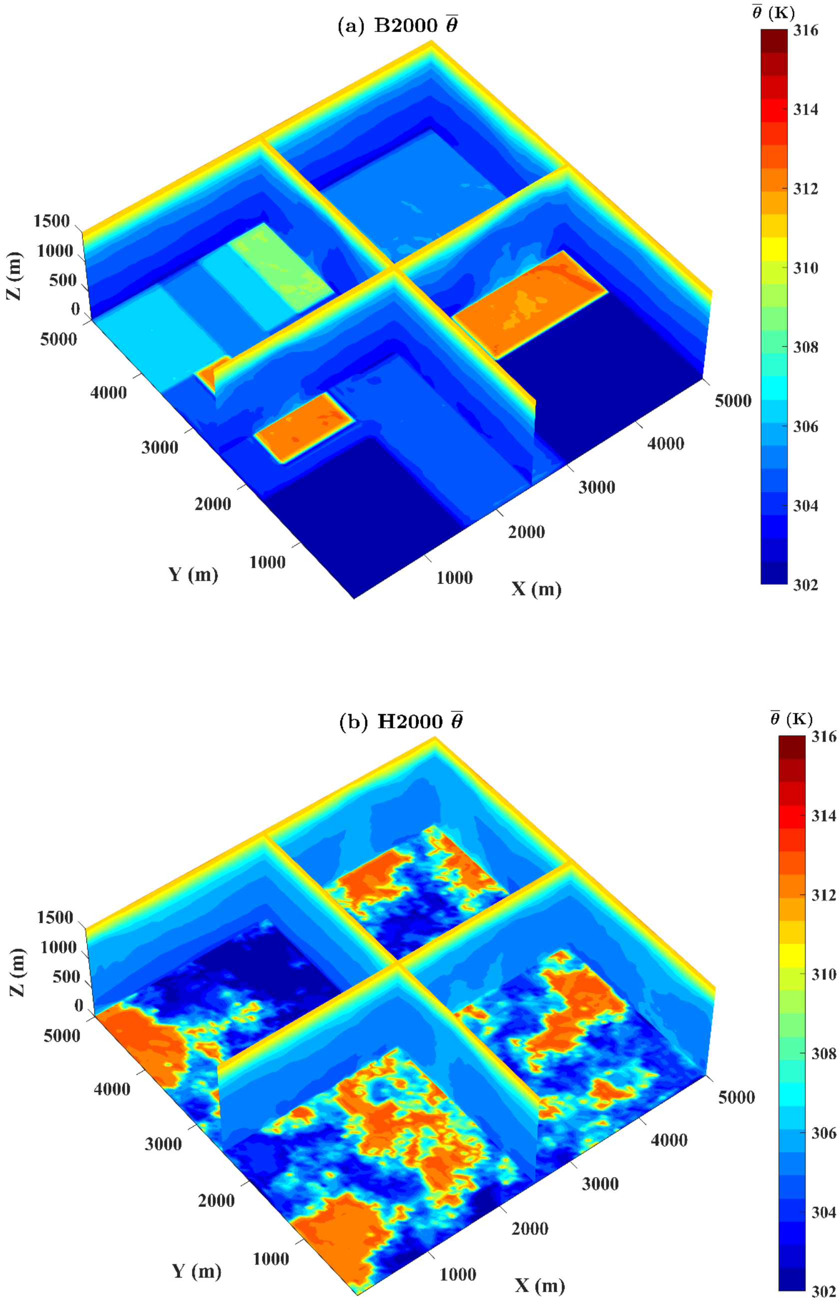

Figure. 3 The temporally averaged potential temperature during the final running hour in case (a) B2000 and (b) H2000. The horizontal slice is at z = 2 m.

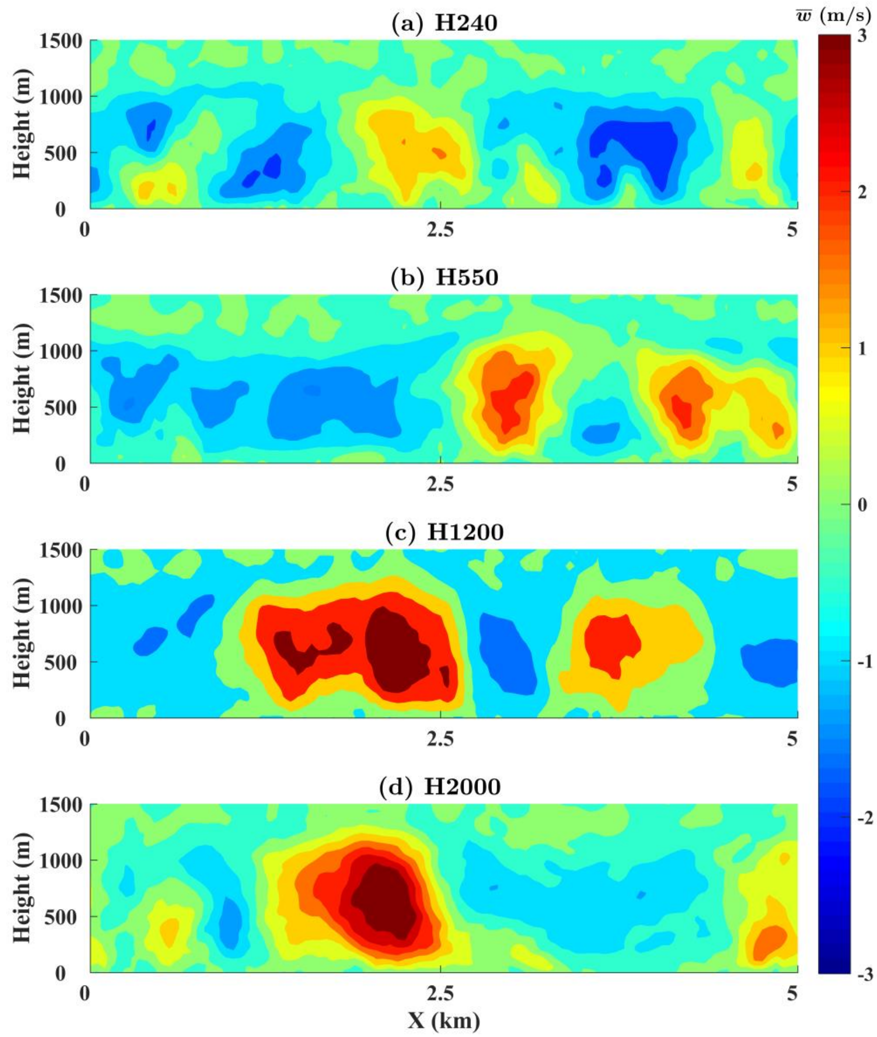

Figure. 4 The cross-sections (*x*-*z*) of temporally averaged vertical velocity during the final running hour in H cases at *y* = 3.5 km.

Figure 5 shows the vertical profiles of mean potential temperature (θ), σ_u^2, σ_w^2, and TKE. The σ_u^2 and σ_w^2 are normalized by w_*^2. Clearly, the cases with the smallest heterogeneity scales (B240 and H240) show structures of a well-mixed CBL. When the heterogeneity scale becomes larger, θ increases with height in the CBL, especially in cases B2000 and H2000. This is in agreement with the results in Raasch and Harbusch (2001) and Avissar and Schmidt (1998). One possible reason is that the asymmetry of circulation within the CBL, i.e., locally restricted updraughts and more extended weaker downdraughts (Deardorff et al., 1969), leads to an increase in θ with z within the CBL. Another possible reason is that when the surface heterogeneity scale is larger, the organized structures generated by the surface heterogeneity have a larger probability to penetrate deeper into the inversion layer than the smaller eddies and hence warmer air is brought downward in the CBL by entrainment, which leads to the larger θ

with higher height, especially when the surface heterogeneous scale is larger than z_i (Fig. 5a). The vertical profiles of σ_u^2 and σ_w^2 indicate characteristics similar to many previous studies (Avissar and Schmidt, 1998; Patton et al., 2005; HM09). Namely, σ_u^2 increases near the surface and the entrainment zone; whereas, σ_w^2 reaches its maximum value at the middle of mixed layer. As the heterogeneity scale becomes larger, σ_w^2 in 0 ~ 0.5 z_i becomes smaller, which is consistent with the results in HM09 and Patton et al. (2005). The main explanation is that the larger surface heterogeneity scale, the more aggregated areas with stronger/weaker heat flux and hence more clearly separated regions with upward and downward eddies (Patton et al., 2005), which reduces the σ_w^2 with large surface heterogeneity scale. Similarly, due to this reason in 0 ~ 0.5 z_i, σ_u^2 generally decreases with increasing heterogeneity scale, which is different from the results in HM09 and Patton et al. (2005), where σ_u^2 increases with increasing surface heterogeneity scale. The free convective atmosphere instead of the shear convective atmosphere in HM09 may be responsible for this difference.

In addition, near the entrainment zone, σ_u^2 increases with increasing surface heterogeneity scale and reaches its maximum value at the heterogeneous scale of 2000 m, which is different from the trend near the surface. This discrepancy could be related to the observed correlation that the larger the surface heterogeneity scale, the larger perturbation induced by entrainment and hence the larger σ_u^2 (Fig. 5b). When the surface heterogeneous scale is larger than z_i, the effects of entrainment on σ_u^2 are maximum and can reach the surface, which leads to a larger σ_u^2 at the heterogeneous scale of 2000 m than that of 1200 m (Fig. 5b). Similarly, due to the effects of entrainment, the height at which the largest σ_w^2 occurs also increases with increasing heterogeneity scale (Fig. 5c).

The profile of TKE is affected by both σ_u^2 and σ_w^2. In general, its value decreases with increasing heterogeneity scale (Fig. 5d). However, it should be noted that near the surface (< 0.1 z_i), the TKE is smallest in cases with heterogeneity scale of 1200 m instead of 2000 m due to the behavior of σ_u^2.

Compared with H cases, θ is smaller in B cases, which is again caused by the different spatial patterns of roughness length and surface temperature (Fig. 2). For example, in the simulation of H2000 (Fig. 2e), the hot patches (higher surface temperature) are located in the center, which induces a relatively smaller extent of weaker downdraughts in the domain. However, in the simulation of B2000, the hot patches are close to the borders (Fig. 2a), which leads to more extended weaker downdraughts in the domain. Because of the more extended weaker downdraughts, the potential temperature is smaller in the simulation of B2000.

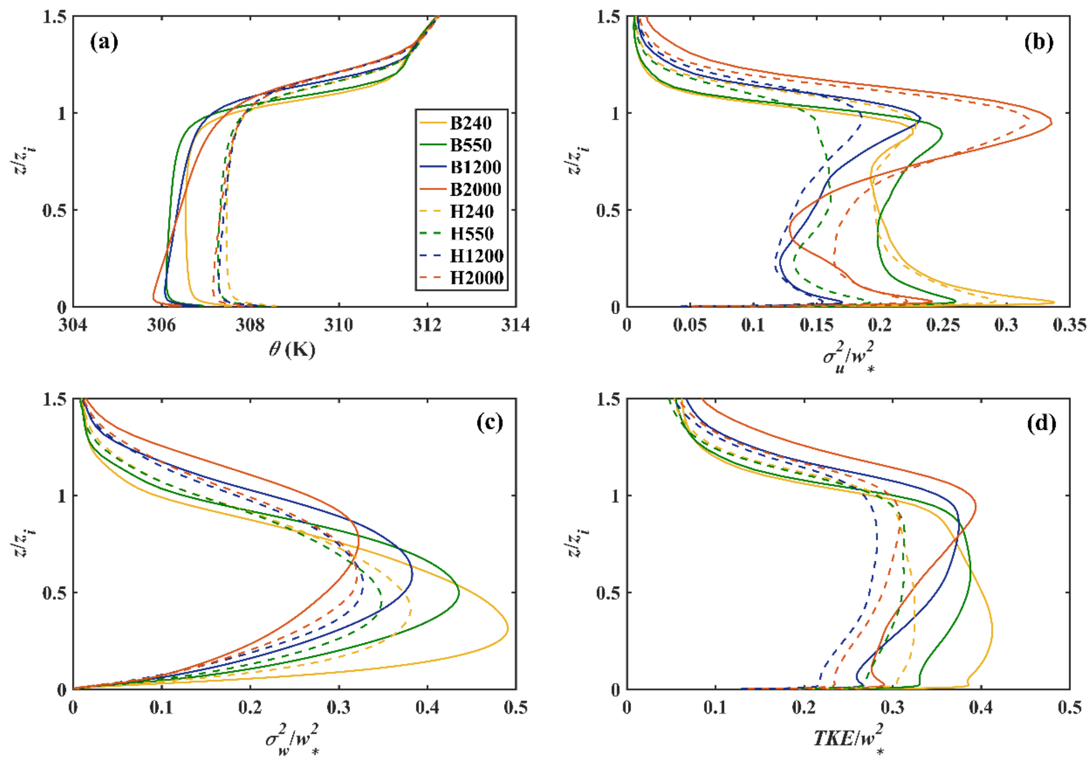

Figure. 5 The vertical profiles of ABL statistics: (a) potential temperature (θ), (b) variance of horizontal velocity (σ_u^2), (c) variance of vertical velocity (σ_w^2), and (d) TKE. All data are averaged in the final hour of simulation and (b, c, d) are normalized by the convective velocity. The boundary-layer height (z_i) is defined as the height where the minimum (negative) value of heat flux is found, and the vertical scale is normalized by z_i in each case.

4.1.2 The flux imbalance

Figure 6(a) shows the vertical profiles of flux imbalance magnitude in different cases. Clearly, the flux imbalance magnitude increases with increasing height in both cases, which is consistent with previous studies (Kanda et al., 2004; Steinfeld et al., 2007; Huang et al., 2008; Zhou et al., 2018). It is also evident that the curves tend to cluster together at lower heights (z/z_i < 0.02). This is due to the fact that the parameterized subgrid-scale turbulence becomes important and the subgrid-scale flux dominates.

To examine the relation between the flux imbalance magnitude and the heteorgeneity scale, the results at 112 m ($z/z_i \approx 0.08$) are shown as an example where the effects of subgrid parameterization should be very small. We choose to analyze the flux imbalance at a fixed z instead of a fixed z/ z_i here because in practice all EC measurements have a fixed z. Overall the flux imbalance magnitude increases with increasing heterogeneity scales, as shown in Fig. 6b. This is consistent with field observations. For example, Stoy et al. (2013) and Xu et al. (2017) found that the flux imbalance magnitude increases with increasing landscape-level and footprint variability, respectively. This can be understood because the larger the heterogeneity scale is, the larger the circulations induced by surface heterogeneity become. These large-scale motions are less likely to be adequately sampled in a finite average period and hence a larger flux imbalance occurs.

Interestingly, when the heterogeneity scale becomes larger than z_i, the flux imbalance magnitude seems to decrease, especially in case B2000 (Fig. 6b). That is, the flux imbalance magnitude reaches its maximum value when the surface heterogeneity scale is about z_i. Close inspection of Fig. 6a reveals that this is the case nearly everywhere as long as $z/z_i > 0.02$. The further reduction of flux imbalance magnitude with increasing heterogeneity scale is probably because the large organized structures generated by the heterogeneity scale of 2000 m can penetrate deeper into the inversion layer and hence warmer air is brought downward into the CBL by entrainment. This additional heat flux caused by entrainment can reach the surface (see Fig. 5a, b), which reduces the flux imbalance magnitude.

In comparison, the flux imbalance in B cases are generally larger than those in H cases. As discussed in Sect. 4.1.1, the smaller TKE and vertical turbulent heat flux induced by the more extended weaker downdraughts in B cases are responsible for this difference.

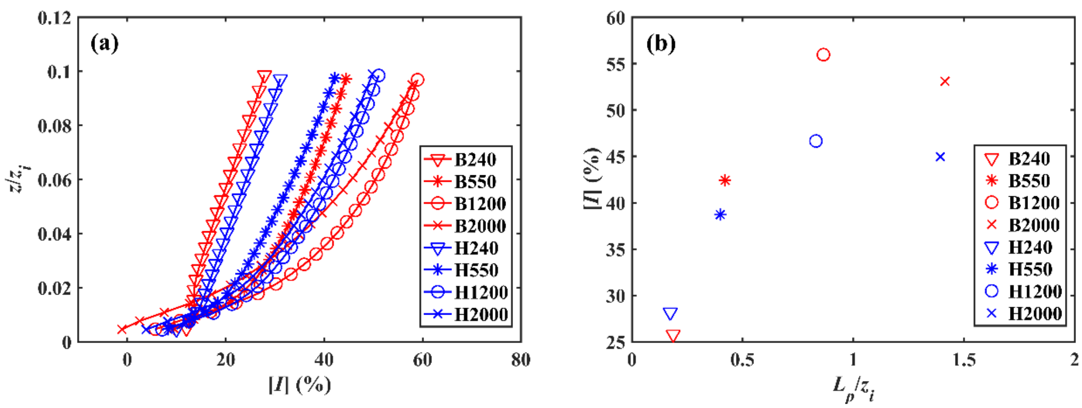

Figure. 6 (a) The vertical profiles of flux imbalance magnitude in different cases; and (b) the flux imbalance magnitude at 112 m as a function of surface heterogeneity scales (L_p) normalized by the boundary layer height (z_i).

4.2 Interpretation of flux imbalance using the cospectral model

The conceptual model described in Sect. 2.3 connects the flux imbalance with f_1 and f_2, where f_1 represents the ratio of “flux at a certain height” to the surface flux and f_2 represents the role of large eddies in inducing flux imbalance. Specifically, the flux imbalance magnitude is expected to increase with decreasing f_1 and f_2. In the following, we investigate the relations between flux imbalance magnitude and f_1 and f_2, as well as their controlling factors.

4.2.1 f_1

The f_1 represents the ratio of the “flux at a certain height” to the surface flux. In the following, the “flux at a certain height” is calculated using the spatial method, i.e., it is the spatial turbulent heat flux calculated at a certain height. Figure 7(a) shows the calculated f_1 at different heights when the subgrid-scale heat flux is included. As can be seen, f_1 deceases with increasing heights in all cases when the subgrid-scale heat flux is included (Fig. 7a). Based on Eq. (11), the decrease of f_1 with increasing heights leads to the increase of flux imbalance magnitude, which is consistent with Fig. 6(a). However, there is virtually no difference between the two cases and also between simulations with different heterogeneity scales. As a result, Fig. 7(a) cannot explain the variations of flux imbalance with respect to heterogeneity scales (Fig. 6b).

Note again that f_1 has large uncertainty at lower heights due to the role of subgrid turbulence parameterization (c.f. Fig. 7a where the subgrid-scale heat flux is included and Fig. 7b where the subgrid-scale heat flux is excluded). For example, near the surface the f_1 values become even larger than 100% when the subgrid-scale flux is included (Fig. 7a), suggesting that the f_1 values at lower heights are less trustable. To avoid the effect of subgrid turbulence parameterization, we will focus on the results in the range of $0.03 < z/z_i < 0.1$ in the following.

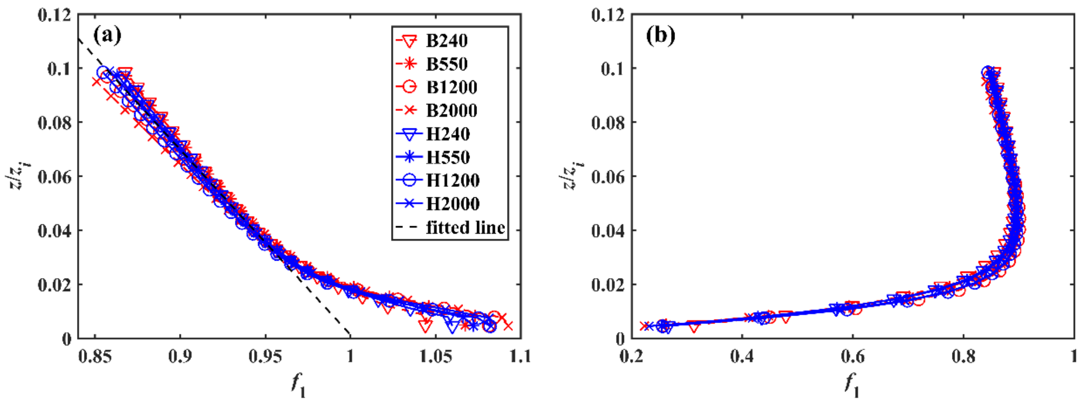

Figure. 7 The vertical profiles of f_1 with (a) the subgrid-scale heat flux included and (b) the subgrid-scale heat flux excluded. The black dash line is the fitted line (see Eq. 14).

4.2.2 f_2

In this section, we examine the relation between f_2, which is inferred from $(1-[I])/f_1$, and different turbulent length scales that might characterize k_{ec}/k_p. Note again that k_{ec} is the critical wavenumber of the EC method and we estimate k_{ec} as $1/(uT)$, where u is a velocity scale that can be represented U, w_*, u_* and $\overline{e}$, and T is the averaging period. The k_p is the peak wavenumber that might be estimated from the integral length scale of vertical velocity (l_w) or the integral length scale of potential temperature (l_θ). In the following we compare all these velocity and length scales.

Figure 8 shows the results in the range of $0.03 < z/z_i < 0.1$ when k_{ec}/k_p is represented by $l_w/(uT)$ with different velocity scales. One can see that f_2 generally decreases with increasing $l_w/(uT)$, consistent with Eq. (11), but with large scatter. Similar results are also found using $l_\theta/(uT)$ and hence those results are not shown. The large scatter suggests that additional variables (e.g., z_i/L) should be considered to include the effects of atmospheric stability on turbulent coherent structures, which are not accounted for by Eq. (11). Similar to previous studies over homogeneous surfaces (Schalkwijk et al., 2016; Huang et al., 2008), we also found a reasonably strong correlation between the flux imbalance magnitude and $-z_i/L$ but over heterogeneous surfaces: the larger the $-z_i/L$, the smaller f_2 and thus the larger the flux imbalance magnitude (Fig. 9).

Therefore, we further examine the correlations between the f_2 and $-z_i/L \times l_w/(uT)$ (Fig. 10). The choice of $-z_i/L \times l_w/(uT)$ is motivated by the fact that the atmospheric stability is likely to influence the largest eddies and may be treated as an adjustable factor to k_p through altering l_w.

Compared to Fig. 8, the negative correlations are much higher in Fig. 10 than those in Fig. 8 (see the R^2 values in Table 3). The better correlations confirm that $-z_i/L$ plays an important role in modulating the flux imbalance over heterogeneous surfaces.

Among all the velocity scales, using $-z_i/L \times l_w/(UT)$ yields the highest R^2 value (Table 3), indicating that the mean horizontal velocity U better characterizes k_{ec}. On the other hand, using l_θ leads to quite parculiar relations and very larger scatter (and thus much smaller R^2 values, not shown here) compared to using l_w (Fig. 11), implying that l_w is a better choice to represent k_p at least in our cases.

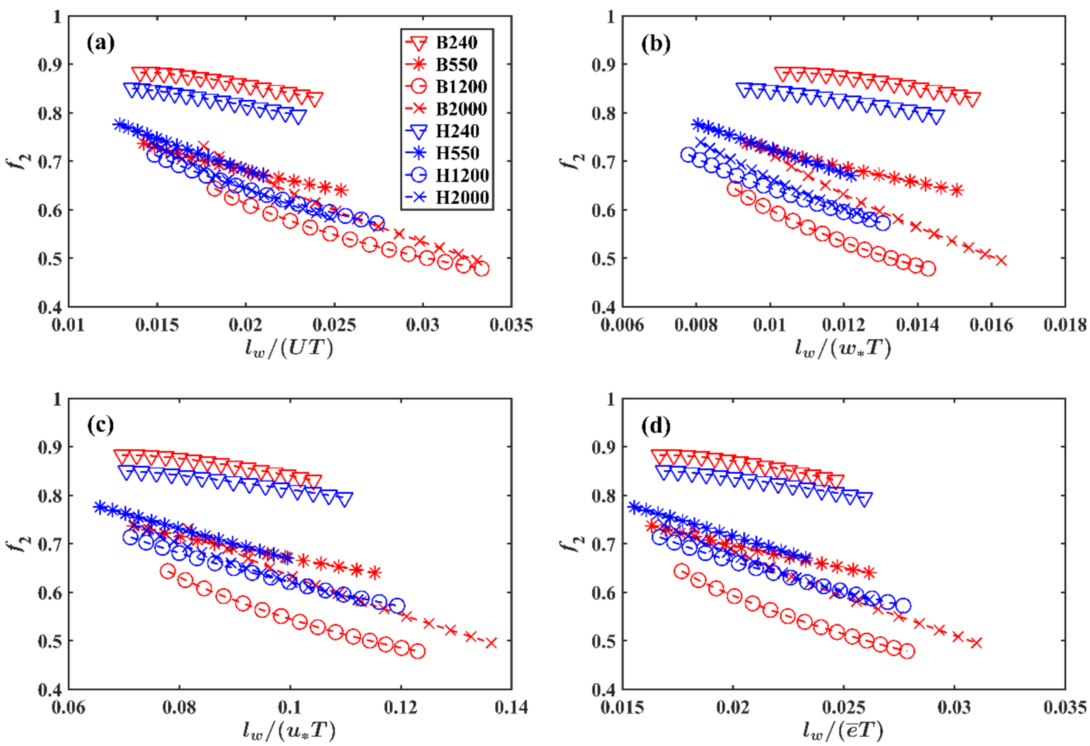

Figure. 8 The relations between f_2 and (a) $l_w/(UT)$, (b) $l_w/(w_*T)$, (c) $l_w/(u_*T)$, and (d) $l_w/(\bar{e}T)$. Only results in the range of $0.03 < z/z_i < 0.1$ are shown.

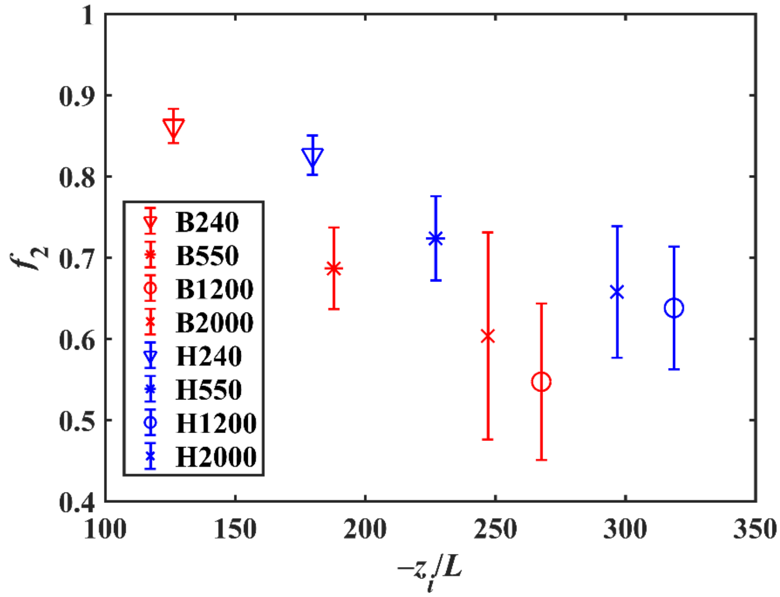

Figure. 9 The f_2 as a function of $-z_i/L$. The marker indicates the mean of results in the range of $0.03 < z/z_i < 0.1$ and the bar indicates the range.

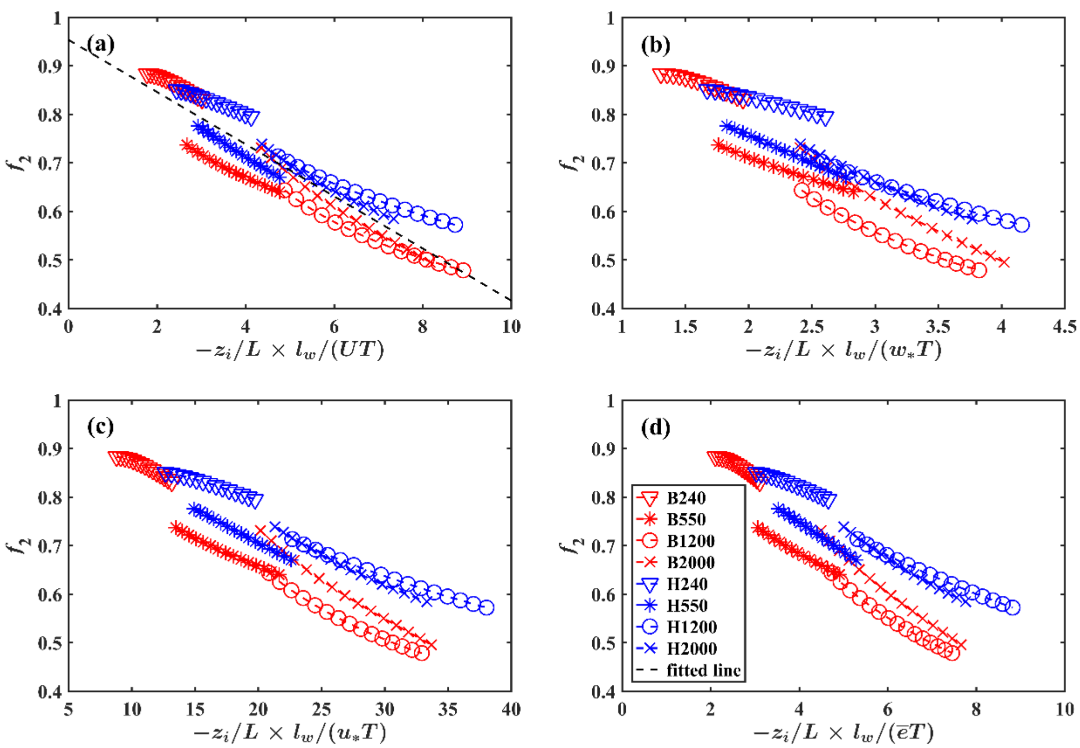

Figure. 10 The relations between f_2 and (a) $-z_i/L \times l_w/(UT)$, (b) $-z_i/L \times l_w/(w_*T)$, (c) $-z_i/L \times l_w/(u_*T)$, and (d) $-z_i/L \times l_w/(\overline{e}T)$. Only results in the range of $0.03 < z/z_i < 0.1$ are shown.

Table 3. The slopes (K), intercepts (C) and coefficients of determination (R^2) between the f_2 and $l_w/(uT)$ (Fig. 8) and $-z_i/L \times l_w/(uT)$ (Fig. 10).

case		$l_w/(UT)$	$l_w/(w_*T)$	$l_w/(u_*T)$	$l_w/(eT)$	$-z_i/L \times l_w/(UT)$	$-z_i/L \times l_w/(w_*T)$	$-z_i/L \times l_w/(u_*T)$	$-z_i/L \times l_w/(\overline{e}T)$
B	K	-19.26	-12.11	-5.47	-22.27	-0.06	-0.16	-0.02	-0.07
	C	1.11	0.83	1.21	1.17	0.96	1.09	1.02	1.03
	R^2	0.78	0.17	0.69	0.62	0.95	0.95	0.97	0.96
H	K	-15.23	-3.89	-3.26	-13.25	-0.05	-0.12	-0.01	-0.05
	C	1.00	0.75	1.00	0.99	0.94	1.03	0.98	0.98
	R^2	0.65	0.08	0.53	0.50	0.93	0.92	0.94	0.94
B + H	K	-16.86	-10.64	-4.54	-18.66	-0.05	-0.14	-0.01	-0.06
	C	1.04	0.82	1.12	1.10	0.95	1.06	0.99	0.98
	R^2	0.74	0.19	0.64	0.58	0.92	0.90	0.89	0.87

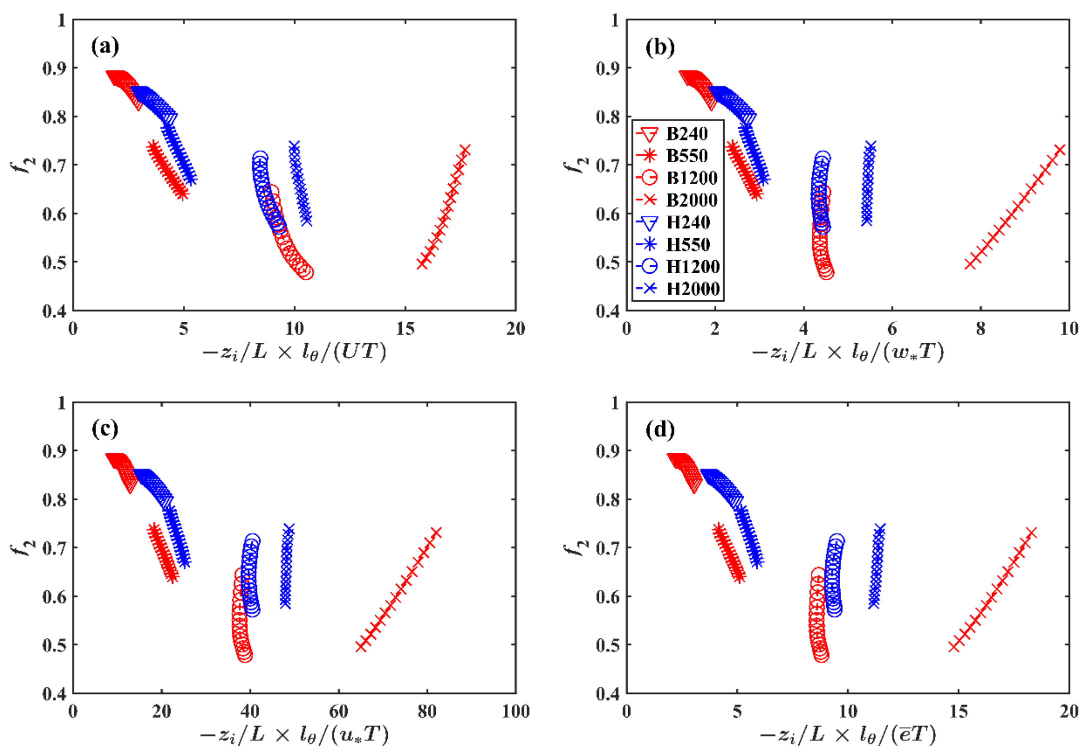

Figure. 11 The relations between f_2 and (a) $-z_i/L \times l_\theta/(UT)$, (b) $-z_i/L \times l_\theta/(w_*T)$, (c) $-z_i/L \times l_\theta/(u_*T)$, and (d) $-z_i/L \times l_\theta/(\overline{e}T)$. Only results in the range of $0.03 < z/z_i < 0.1$ are shown.

4.2.3 A diagnostic equation for [I]

Given that the behavior of f_1 with z is quite predictable from Fig. 7, f_1 may be parameterized as follows:

$$f_1 = a\frac{z}{z_i} + b, \tag{14}$$

where a = -1.46 and b =1.0 are fitted parameters (see the fitted line in Fig. 7). Again, to avoid the effect of subgrid turbulence parameterization, only data betwee in the range of $0.03 < z/z_i < 0.1$ are used to fit the parameters in Eq. (14). The linear decrease of turbulent heat flux in the CBL is a well-established result (Garratt 1992), and our results confirms this. Note that we did not *a priori* specify the value of b. The fact that $b = 1.0$ is obtained from the fitting demonstrates that the linear decreasing trend in the range of $0.03 < z/z_i < 0.1$, when extrapolated to the surface, recovers the surface heat flux.

Similarly, given the nearly linear relationship between f_2 and $-z_i/L \times l_w/(UT)$ (here we use U due to the largest R^2 value it yields as shown in Table 3 and also the fact that its measurement is often available), we can parameterize f_2 as

$$f_2 = K\frac{z_i}{L}\frac{l_w}{UT} + C, \tag{15}$$

where K = -0.05 and C = 0.95 are fitted parameters (see the fitted line in Fig. 10a). Based on Eqs. (7), (14), (15), the flux imbalance magnitude can be parameterized as follows:

$$[I] = 1 - \left[a\frac{z}{z_i} + b\right]\left[K\frac{z_i}{L}\frac{l_w}{UT} + C\right]. \tag{16}$$

In practice, some of the inputs for Eq. (16) are not always available even if the coefficients a, b, K, and C are provided by fitting to LES results. For example, the calculation of z_i/L requires the boundary layer height and the surface heat flux. The former is rarely measured in the field while the latter is what the EC aims to measure and thus is unknown *a priori*. From this point view, Eq. (16) is a *diagnostic* eqution and cannot be used as a *prognostic* equation to compute the flux imbalance. We note that this is also the case for other parameterizations in the literature (see e.g., Huang et al., 2008).

5 Discussion

5.1 The relation between the surface heterogeneity scale and flux imbalance

Our results demonstrate that the following variables primarily affect the flux imbalance: the integral length scale of vertical velocity l_w, the atmospheric stability parameter z_i/L, the mean horizontal velocity U, and the average period T, when the cospectral model is employed to interpret the flux imbalance. Among these four variables, l_w determines the maximum size of large-scale turbulent structures (i.e., the large eddies), z_i/L affects the shape of these turbulent structures and also the cospectrum form, i.e., the flux distribution among different eddy sizes, whereas U and T determine the number of large eddies that can be sampled by the EC sensors in a finite averaging period.

These characteristic variables are strongly affected by the surface heterogeneity. For example, one can infer from Fig. 9 that z_i/L is dependent on the surface heterogeneity scale. Figure 12a shows this more clearly. In addition, Fig. 12b shows the dependence of $l_w/(UT)$ on the surface heterogeneity scale. Due to the dependence of these characteristic variables on the surface heterogeneity scale, the flux imbalance is shown to be affected by surface heterogeneity in both our simulations (Fig. 6b) and previous observational studies (Stoy et al., 2013; Xu et al., 2017). Our results demonstrate that although the pdf of surface characteristics remains identical, landscapes with different characteristic length scales can have vastly different flux imbalance magnitude. This may explain why the relation between the surface heterogeneity and the flux imbalance observed in the field data shows large variability (Stoy et al., 2013; Xu et al., 2017).

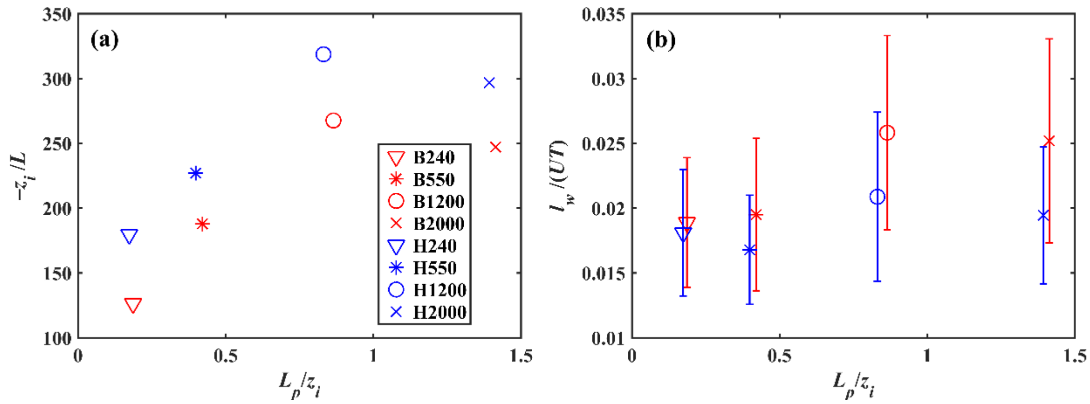

Figure. 12 The (a) $-z_i/L$ and (b) $l_w/(UT)$ as a function of L_p/z_i. The marker in (b) indicates the mean of results in the range of $0.03 < z/z_i < 0.1$ and the bar in (b) indicates the range.

5.2 The relations between the Eq. (16) and related factors

As stated in the introduction, previous studies have reported relations between flux imbalance and various factors (see Table 1). In this section, we use the conceptual model (i.e., Eq. 16) to explain these reported relations in the literature imbalance. Based on Eq. (16), it can be easily seen that the flux imbalance *I* increases with increasing *z* and $-z_i/L$, decreasing *U* (when *u* is represented by *U*) and TKE (when *u* is represented by TKE), and shorter *T*. Due to the increasing of *I* with *z* and $-z_i/L$, *I* also increases with the increasing of $-z/L$. In addition, as discussed in Sect. 5.1 and shown in Sect. 4.1.2 (Fig. 6b), oveall the flux imbalance *I* increases with increasing surface heterogeneity scale. Because the $-z_i/L$ can be expressed as follows:

$$-\frac{z_i}{L} = k\left(\frac{w_*}{u_*}\right)^3, \tag{17}$$

where *k* is the von-Karman constant. Based on Eq. (17) and Eq. (16), we can also see that the flux imbalance *I* increases with decreasing u_*/w_*. These results inferred from our conceptual model are consistent with previous studies (see Table 1).

Furthermore, we can express Eq. (9) as follows:

$$f_2 = 1 - \frac{\int_0^{k_{ec}} F_{w\theta}(k,z)\,dk}{\int_0^{\infty} F_{w\theta}(k,z)\,dk} = 1 - \frac{1}{R_{w\theta}(z)\sigma(w)\sigma(\theta)}\int_0^{k_{ec}} F_{w\theta}(k,z)\,dk, \tag{18}$$

where $R_{w\theta}(z)$ is the correlation coefficient between *w* and θ at *z*; $\sigma(w)$ and $\sigma(\theta)$ are standard deviations of *w* and θ, respectively. A larger phase difference between *w* and θ results in a smaller $R_{w\theta}$ and thus a smaller f_2 (Eq. 18), which leads to a larger *I* based on Eq. (7). This conclusion is consistent with results in McGloin et al. (2018) and Gao et al. (2017).

In summary, with the proposed diagnostic equation for *I* (i.e., Eq. 16), the relations between the flux imbalance and various factors reporeted in the literature (see Table 1) can be all explained.

5.3 A comparison of different parameterizations for flux imbalance

Several energy balance closure parametrization schemes have been proposed (Panin et al., 1998; Huang et al., 2008; Panin and Bernhofer, 2008). In this paper, we also propose a conceptual model to explain the flux imbalance. Here, we compare these models and explain their advantages and limitations.

Based on LES runs over homogeneous surfaces, Huang et al. (2008) parametrized the flux imbalance as a function of non-dimensionalized turbulent velocity scales as

$$[I] = \left[\exp^{\left(a+b\frac{u_*}{w_*}\right)} + c\right]\left[1.1 + d\left(\frac{z}{z_i} + f\right)^2\right]^{0.5}, \tag{19}$$

where a = 4.2, b = –16, c = 2.1, d = –8.0 and f = –0.38 are fitted parameters. It has been found the biggest shortcoming of this empirical parametrization scheme is that it cannot be applied directly to heterogeneous surfaces (Zhou et al., 2018). Considering that surface heterogeneity is one of the main contributors to flux imbalance, the applicability of this parametrization scheme is greatly limited. In addition, this parameterization is developed based on LES data above the surface layer ($0.3 < z/z_i < 0.5$) and hence its applicability for analyzing real observations, which are mostly collected in the surface layer, is questionable. This may be why field observations have reported failure of using this relation to capture flux imbalance (Eder et al., 2014). Lastly, as alluded to earlier, this parameterization cannot be used as a prognostic equation since one of the required inputs is the surface heat flux for computing w_*.

To consider the effect of surface heterogeneity on the flux imbalance, Panin and Bernhofer (2008) directly related the effective surface roughness length (z_0^{eff}) and surface heterogeneity scale (i.e., L^{eff}) to the flux imbalance and proposed the following parameterization

$$EBR = 1 - [I] = K\frac{z_0^{eff}}{L^{eff}} + C, \tag{20}$$

where EBR is the energy-balance closure ratio (the ratio of the sum of turbulent heat fluxes to the available energy), and K and C are empirical constants. Compared to the parameterization by Huang et al. (2008), the biggest advantage of this empirical parametrization scheme is that it explicitly considers the effects of surface heterogeneity and hence it can be used over heterogeneous surfaces. However, there are also some limitations associated with this parameterization. First, only the effect of momentum roughness length is included. Second, as shown in Fig. 6, even the same surface heterogeneity scale can yield very different flux imbalance magnitude. The large variation of flux imbalance magnitude suggests that the empirical constants (i.e., K and C) may be varying across sites and hence it is not surprising that the performance of this model also varies across sites (Eder et al., 2014). Last, the atmospheric stability and its interaction with surface heterogeneity can strongly affect turbulent organized structures, which further alters the flux imbalance. Hence, only considering the surface heterogeneity scale cannot correctly capture the flux imbalance under a variety of atmospheric stability conditions.

Compared to the previous two models, our model is derived from the cospectrum and hence is more physically based. It should be pointed out that the surface heterogeneity scale is not explicit in our model. This is because the model is constructed based on the assumption that large-scale organized turbulent structures lead to the flux imbalance. The effect of surface heterogeneity on flux imbalance is implicitly included in our model by considering the impact of surface heterogeneity on characteristic variables of turbulent flows, especially those related to large eddies.

There are also some limitations of our model. Most importantly, our model is based on the assumption that the flux imbalance is only caused by the large eddies. Therefore, the flux imbalance caused by other factors cannot be explained by our model. In addition, our model is also a diagnostic model and cannot be directly applied in practice to calculate the flux imbalance. Lastly, our model is constructed with data in the range $0.03 < z/z_i < 0.1$. While this range is much lower than that in Huang et al. (2008), the lowest limit ($z/z_i = 0.03$) is still higher than the typical measurement height in the field. Whether our model can capture the behavior of flux imbalance near the surface ($z/z_i < 0.03$) needs to be investigated using higher-resolution LES simulations in the future.

6 Conclusions

This study analyzes the relationship between the surface heterogeneity scale and the flux imbalance over heterogeneous landscapes in a dry convective boundary layer. The main conclusions are summarized as follows:

(1) The surface heterogeneity scale strongly affects the flux imbalance even when the pdfs of surface characteristics are the same. The flux imbalance magnitude initially increases with increasing surface heterogeneity scale and reaches its peak value when the surface heterogeneity scale is similar to the boundary-layer height z_i. When the surface heterogeneity scale is larger than z_i, the organized structures can penetrate deeper into the inversion layer and hence warmer air is brought downward in the CBL by entrainment. This additional heat flux reduces the flux imbalance magnitude to a certain degree.

(2) A conceptual model for the flux imbalance is proposed to better understand the flux imbalance induced by the large eddies. Based on this conceptual model, we find that z_i/L, l_w, U, and T are the key variables that control the flux imbalance. Among these three variables, the l_w determines the maximum size of large eddies; the z_i/L represents the form of these large eddies or the cospectrum form, i.e., the flux distribution among different eddy sizes; the U and T determine the numbers of these large eddies can be sampled by the EC in a finite averaging period.

(3) Assuming that the flux imbalance is mainly caused by the inadequate sampling of large eddies, a diagnostic equation for the flux imbalance magnitude is proposed as $[I] = 1\text{-}[az/z_i + b][-K \times z_i/L \times l_w/UT + C]$, where a, b, K, and C are empirical constants and b should in theory equal to unity. Compared to the other empirical and semi-empirical models, our model is derived from the cospectrum and hence is more physically based. Moreover, the relations between the flux imbalance and various factors reported in the literature can be explained by our model. Note that our model is diagnostic because it requires *a priori* knowledge of the surface heat flux. In addition, it also requires boundary-layer height as an input, which is not always available. It is also pointed out that this model is constructed with data in the range $0.03 < z/z_i < 0.1$.

Our study has a few limitations that should be pointed out. First, it is important to point out that our study does not consider latent heat flux, whose behavior might be different from that of sensible heat flux, especially in the low frequency (Cava et al., 2008; Detto et al., 2008; Huang et al., 2009; Li and Bou-Zeid, 2011; Li et al., 2012; Cancelli et al., 2014; Charuchittipan et al., 2014; Gao et al., 2017). Second, we only examine the flux imbalance under free convective conditions and the effect of wind remains to be investigated. Last, it is noted that we use the control volume method (i.e., a regular control volume) to calculate the flux imbalance. However, in the field, the footprint of EC is not a rectangle and varies with the wind and atmospheric stability. The effect of this mismatch between the regular control volume and the irregular footprint (Metzger, 2018) on flux imbalance needs to be investigated in the future.

Appendix A: The derivation of Eq. (11)

In this appendix, the flux imbalance is deduced by using the cospectral model of Lee et al. (2005), which can be expressed as follows:

$$F_{w\theta}(k) = \frac{A_{w\theta}}{k_p\left[1 + m_{w\theta}\left(\frac{k}{k_p}\right)^{2\mu}\right]^{\frac{1}{2\mu}\frac{m_{w\theta}+1}{m_{w\theta}}}}, \tag{21}$$

where $A_{w\theta}$ is a normalization parameter, k_p is the peak wavenumber, and $m_{w\theta}$ and μ are the (inertial subrange) slope parameter and broadness parameter, respectively. Substituting Eq. 21 into the Eq. (9), the flux imbalance can be expressed as:

$$f_2 = 1 - \frac{\dfrac{D\Gamma\left(\frac{1}{2\mu}, 0\right) - D\Gamma\left(\frac{1}{2\mu}, \frac{m+1}{2\mu}\left(\frac{k_{ec}}{k_p}\right)^{2\mu}\right)}{(1+m)^{\frac{1}{2\mu}}}}{\dfrac{D\Gamma\left(\frac{1}{2\mu}, 0\right)}{(1+m)^{\frac{1}{2\mu}}}} = \frac{\Gamma\left(\frac{1}{2\mu}, \frac{m+1}{2\mu}\left(\frac{k_{ec}}{k_p}\right)^{2\mu}\right)}{\Gamma\left(\frac{1}{2\mu}, 0\right)}, \tag{22}$$

where

$$D = 2^{\frac{1}{2\mu}-1} a\, \mu^{\frac{1}{2\mu}-1}, \tag{23}$$

$$\Gamma(s, x) = \int_x^{\infty} t^{s-1} e^{-t}\, dt. \tag{24}$$

Eq. (22) is identical to the Eq. (11) in the main text. Due to the decrease of $\Gamma(s, x)$ with increasing x, f_2 is expected to decrease as k_{ec}/k_p increases.

Appendix B: Different cospectral models and the derived f_2

In this appendix, different cospectral models are used to derive the flux imbalance.

1 The cospectral model of Katul et al. (2013)

Katul et al. (2013) provided a simple cospectral model, which can be expressed as follows:

$$F_{w\theta}(k)=\begin{cases}\dfrac{\varepsilon^{-\frac{1}{3}}k_p^{-\frac{7}{3}}}{C_1}\{dTC_{ww}+(1-C_2)\beta C_{\theta\theta}\}, & k>k_p\\ \dfrac{\varepsilon^{-\frac{1}{3}}k^{-\frac{7}{3}}}{C_1}\{dTC_{ww}+(1-C_2)\beta C_{\theta\theta}\}, & k\le k_p\end{cases},\qquad 25)$$

where ε is the TKE dissipation rate; k_p is the peak wavenumber; dT and β are the air temperature gradient and buoyancy parameter, respectively; and C_2, C_{ww} and $C_{\theta\theta}$ are constants. Substituting Eq. 25 into the Eq. (9), the flux imbalance leads to:

$$f_2=1-\frac{\dfrac{k_{ec}\varepsilon^{-\frac{1}{3}}k_p^{-\frac{7}{3}}}{C_1}\{\Gamma C_{ww}+(1-C_2)\beta C_{\theta\theta}\}}{\dfrac{7}{4}k_p^{-\frac{4}{3}}\dfrac{\varepsilon^{-\frac{1}{3}}}{C_1}\{\Gamma C_{ww}+(1-C_2)\beta C_{\theta\theta}\}}=1-\frac{4}{7}\frac{k_{ec}}{k_p}.\qquad 26)$$

Clearly, f_2 decreases with increasing k_{ec}/k_p.

2 The cospectral model of Massom and Lee (2002)

Massom and Lee (2002) gave another simple expression for cospectrum:

$$F_{w\theta}(k)=\frac{2}{\pi}\frac{1}{k_p[1+(k/k_p)]^2}.\qquad (27)$$

Substituting Eq. 27 into Eq. (9), f_2 can be expressed as follows:

$$f_2=\frac{1}{\left(1+\dfrac{k_{ec}}{k_p}\right)}.\qquad 28)$$

It is clear that in this model f_2 also decreases with increasing k_{ec}/k_p.

Acknowledgments

This work was jointly supported by the National Natural Science Foundation of China (Grant: 91425303) and the inter-disciplinary Innovation Team of the Chinese Academy of Science (Grant: XXH13505-06). The authors declare that they have no conflict of interest. All data used in this study can be obtained from the Environmental and Ecological Science Data Center for West China (http://westdc.westgis.ac.cn).

References

Albertson, J. D., W. P. Kustas, and T. M. Scanlon (2001), Large-eddy simulation over heterogeneous terrain with remotely sensed land surface conditions, Water Resources Research, 37(7), 1939-1953, doi: 10.1029/2000wr900339.

Aubinet, M., T. Vesala, and D. Papale (2012), Eddy Covariance, in A Practical Guide to Measurement and Data Analysis, edited by M. Aubinet, T. Vesala and D. Papale, p. 442, Springer, Dordrecht, Heidelberg, London, New York, doi:0.1007/978-94-007-2351-1.

Avissar, R., and T. Schmidt (1998), An evaluation of the scale at which ground-surface heat flux patchiness affects the convective boundary layer using large-eddy simulations, Journal of the Atmospheric Sciences, 55(16), 2666-2689, doi:10.1175/1520-0469(1998)055<2666:aeotsa>2.0.co;2.

Bertoldi, G., J. D. Albertson, W. P. Kustas, F. Li, and M. C. Anderson (2007), On the opposing roles of air temperature and wind speed variability in flux estimation from remotely sensed land surface states, Water Resources Research, 43(10), W10433, doi:10.1029/2007wr005911.

Bou-Zeid, E., M. B. Parlange, and C. Meneveau (2007), On the parameterization of surface roughness at regional scales, Journal of the Atmospheric Sciences, 64(1), 216-227, doi:10.1175/Jas3826.1.

Cancelli, D. M., M. Chamecki, and N. L. Dias (2014), A Large-Eddy Simulation Study of Scalar Dissimilarity in the Convective Atmospheric Boundary Layer, Journal of the Atmospheric Sciences, 71(1), 3-15, doi:10.1175/jas-d-13-0113.1.

Charuchittipan, D., W. Babel, M. Mauder, J.-P. Leps, and T. Foken (2014), Extension of the averaging time in eddy-covariance measurements and its effect on the energy balance closure, Boundary-Layer Meteorology, 152(3), 303-327, doi:10.1007/s10546-014-9922-6.

Chen, F., and R. Avissar (1994), The impact of land-surface wetness heterogeneity on mesoscale heat fluxes, Journal of Applied Meteorology, 33(11), 1323-1340, doi:10.1175/1520-0450(1994)033<1323:tiolsw>2.0.co;2.

Chen, J., S. Fan, C. Zhao, X. Xiao, X. Cai, and H. Liu (2006), The underestimation of the turbulent fluxes in eddy correlation techniques, Chinese Journal of Atmospheric Sciences, 03, 423-432, doi:10.3878/j.issn.1006-9895.2006.03.06. (in Chinese)

De Roo, F., and M. Mauder (2018), The influence of idealized surface heterogeneity on virtual turbulent flux measurements, Atmospheric Chemistry and Physics, 18(7), 5059-5074, doi:10.5194/acp-18-5059-2018.

Deardorff, J. W., G. E. Willis, and D. K. Lilly (1969), Laboratory investigation of non-steady penetrative convection, Journal of Fluid Mechanics, 35, 7-31, doi:10.1017/S0022112069000942.

Dennis, D. J. C., and T. B. Nickels (2008), On the limitations of Taylor's hypothesis in constructing long structures in a turbulent boundary layer, Journal of Fluid Mechanics, 614, 197-206, doi:10.1017/S0022112008003352.

Detto, M., G. Katul, M. Mancini, N. Montaldo, and J. D. Albertson (2008), Surface heterogeneity and its signature in higher-order scalar similarity relationships, Agricultural and Forest Meteorology, 148(6-7), 902-916, doi:10.1016/j.agrformet.2007.12.008.

Eder, F., F. De Roo, K. Kohnert, R. L. Desjardins, H. P. Schmid, and M. Mauder (2014), Evaluation of two energy balance closure parametrizations, Boundary-Layer Meteorology, 151(2), 195-219, doi:10.1007/s10546-013-9904-0.

Eder, F., M. Schmidt, T. Damian, K. Traumner, and M. Mauder (2015a), Mesoscale eddies affect near-surface turbulent exchange: evidence from lidar and tower measurements, Journal of Applied Meteorology and Climatology, 54(1), 189-206, doi:10.1175/Jamc-D-14-0140.1.

Eder, F., F. De Roo, E. Rotenberg, D. Yakir, H. P. Schmid, and M. Mauder (2015b), Secondary circulations at a solitary forest surrounded by semi-arid shrubland and their impact on eddy-covariance measurements, Agricultural and Forest Meteorology, 211, 115-127, doi:10.1016/j.agrformet.2015.06.001.

Finnigan, J. J., R. Clement, Y. Malhi, R. Leuning, and H. A. Cleugh (2003), A re-evaluation of long-term flux measurement techniques - Part I: Averaging and coordinate rotation, Boundary-Layer Meteorology, 107(1), 1-48, doi:10.1023/A:1021554900225.

Foken, T. (2008), The energy balance closure problem: An overview, Ecological Applications, 18(6), 1351-1367, doi:10.1890/06-0922.1.

Foken, T., M. Aubinet, J. J. Finnigan, M. Y. Leclerc, M. Mauder, and K. T. P. U (2011), Results of a panel discussion about the energy balance closure correction for trace gases, Bulletin of the American Meteorological Society, 92(4), Es13-Es18, doi:10.1175/2011bams3130.1.

Foken, T., F. Wimmer, M. Mauder, C. Thomas, and C. Liebethal (2006), Some aspects of the energy balance closure problem, Atmospheric Chemistry and Physics, 6, 4395-4402.

Franssen, H. J. H., R. Stöckli, I. Lehner, E. Rotenberg, and S. I. Seneviratne (2010), Energy balance closure of eddy-covariance data: A multisite analysis for European FLUXNET stations, Agricultural and Forest Meteorology, 150(12), 1553-1567, doi:10.1016/j.agrformet.2010.08.005.

Gao, Z. M., H. P. Liu, G. K. Katul, and T. Foken (2017), Non-closure of the surface energy balance explained by phase difference between vertical velocity and scalars of large atmospheric eddies, Environmental Research Letters, 12(3), 034025, doi:10.1088/1748-9326/aa625b.

Gao, Z.Q., R. Horton, and H. P. Liu (2010), Impact of wave phase difference between soil surface heat flux and soil surface temperature on soil surface energy balance closure, Journal of Geophysical Research-Atmospheres, 115, D16112, doi:10.1029/2009jd013278.

Garratt JR (1992) The atmospheric boundary layer. Cambridge University Press, UK 316 pp

Huang, H.-Y., and S. A. Margulis (2009), On the impact of surface heterogeneity on a realistic convective boundary layer, Water Resources Research, 45(4), W04425, doi:10.1029/2008WR007175.

Huang, J. P., X. H. Lee, and E. G. Patton (2008), A modelling study of flux imbalance and the influence of entrainment in the convective boundary layer, Boundary-Layer Meteorology, 127(2), 273-292, doi:10.1007/s10546-007-9254-x.

Huang, J. P., X. H. Lee, and E. G. Patton (2009), Dissimilarity of scalar transport in the convective boundary layer in inhomogeneous landscapes, Boundary-Layer Meteorology, 130(3), 327-345, doi:10.1007/s10546-009-9356-8.

Inagaki, A., M. O. Letzel, S. Raasch, and M. Kanda (2006), Impact of surface heterogeneity on energy imbalance: A study using LES, Journal of the Meteorological Society of Japan, 84(1), 187-198, doi:10.2151/jmsj.84.187.

Jung, M., M. Reichstein, P. Ciais, S. I. Seneviratne, J. Sheffield, M. L. Goulden, G. Bonan, A. Cescatti, J. Chen, and R. De Jeu (2010), Recent decline in the global land evapotranspiration trend due to limited moisture supply, Nature, 467(7318), 951-954, doi:10.1038/nature09396.

Kaimal, J. C., J. C. Wyngaard, D. A. Haugen, O. R. Coté, Y. Izumi, S. J. Caughey, and C. J. Readings (1976), Turbulence structure in the convective boundary layer, Journal of the Atmospheric Sciences, 33(11), 2152-2169, doi:10.1175/1520-0469(1976)033<2152:tsitcb>2.0.co;2.

Kaimal JC, Finnigan JJ (1994) Atmospheric boundary layer flows: their structure and measurement. Oxford University Press, New York, 289 pp

Kanda, M., A. Inagaki, M. O. Letzel, S. Raasch, and T. Watanabe (2004), LES study of the energy imbalance problem with eddy covariance fluxes, Boundary-Layer Meteorology, 110(3), 381-404, doi:DOI 10.1023/B:BOUN.0000007225.45548.7a.

Katul, G. G., A. Porporato, C. Manes, and C. Meneveau (2013), Co-spectrum and mean velocity in turbulent boundary layers, Physics of Fluids, 25(9), 091702, doi:10.1063/1.4821997.

Khanna, S., and J. G. Brasseur (1998), Three-dimensional buoyancy- and shear-induced local structure of the atmospheric boundary layer, Journal of the Atmospheric Sciences, 55(5), 710-743, doi:10.1175/1520-0469(1998)055<0710:tdbasi>2.0.co;2.

Kustas, W. P., and J. D. Albertson (2003), Effects of surface temperature contrast on land-atmosphere exchange: A case study from Monsoon 90, Water Resources Research, 39(6), 1159, doi:10.1029/2001wr001226.

Lee, X. H. (1998), On micrometeorological observations of surface-air exchange over tall vegetation, Agricultural and Forest Meteorology, 91(1-2), 39-49, doi:10.1016/S0168-1923(98)00071-9.

Lee, X. H., W. Massman, and B. Law (2005), Handbook of micrometeorology-A guide for surface flux measurement and analysis, 250 pp., Springer Netherlands, doi:10.1007/1-4020-2265-4.

Lenschow, D. H., and B. B. Stankov (1986), Length scales in the convective boundary layer, Journal of the Atmospheric Sciences, 43(12), 1198-1209, doi:10.1175/1520-0469(1986)043<1198:Lsitcb>2.0.Co;2.

Leuning, R., E. van Gorsel, W. J. Massman, and P. R. Isaac (2012), Reflections on the surface energy imbalance problem, Agricultural and Forest Meteorology, 156, 65-74, doi:10.1016/j.agrformet.2011.12.002.

Li, D., and E. Bou-Zeid (2011), Coherent structures and the dissimilarity of turbulent transport of momentum and scalars in the unstable atmospheric surface layer, Boundary-Layer Meteorology, 140(2), 243-262, doi:10.1007/s10546-011-9613-5.

Li, D., E. Bou-Zeid, and H. A. R. De Bruin (2012), Monin-Obukhov similarity functions for the structure parameters of temperature and humidity, Boundary-Layer Meteorology, 145(1), 45-67, doi:10.1007/s10546-011-9660-y.

Li, D., and G. G. Katul (2017), On the linkage between the $k^{-5/3}$ spectral and $k^{-7/3}$ cospectral scaling in high-Reynolds number turbulent boundary layers, Physics of Fluids, 29(6), 065108, doi:10.1063/1.4986068.

Li, Z. Q., G. R. Yu, X. F. Wen, L. M. Zhang, C. Y. Ren, and Y. L. Fu (2005), Energy balance closure at ChinaFLUX sites, Science in China Series D-Earth Sciences, 48, 51-62, doi:10.1360/05zd0005.

Liu, S. F., Y. P. Shao, A. Kunoth, and C. Simmer (2017), Impact of surface-heterogeneity on atmosphere and land-surface interactions, Environmental Modelling & Software, 88, 35-47, doi:10.1016/j.envsoft.2016.11.006.

Lumley, J. L. (1967), Similarity and the Turbulent Energy Spectrum, Physics of Fluids, 10(4), 855-858, doi:10.1063/1.1762200.

Mahrt, L. (1998), Flux sampling errors for aircraft and towers, Journal of Atmospheric and Oceanic Technology, 15(2), 416-429, doi:10.1175/1520-0426(1998)015<0416:Fsefaa>2.0.Co;2.

Massman, W. J., and X. Lee (2002), Eddy covariance flux corrections and uncertainties in long-term studies of carbon and energy exchanges, Agricultural and Forest Meteorology, 113(1-4), 121-144, doi:10.1016/S0168-1923(02)00105-3.

McGloin, R., L. Šigut, K. Havránková, J. Dušek, M. Pavelka, and P. Sedlák (2018), Energy balance closure at a variety of ecosystems in Central Europe with contrasting topographies, Agricultural and Forest Meteorology, 248, 418-431, doi:10.1016/j.agrformet.2017.10.003.

Metzger, S. (2018), Surface-atmosphere exchange in a box: Making the control volume a suitable representation for in-situ observations, Agricultural and Forest Meteorology, 255, 68-80, doi:10.1016/j.agrformet.2017.08.037.

Moeng, C. H., and P. P. Sullivan (1994), A comparison of shear-driven and buoyancy-driven planetary boundary-layer flows, Journal of the Atmospheric Sciences, 51(7), 999-1022, doi:Doi 10.1175/1520-0469(1994)051<0999:Acosab>2.0.Co;2.

Moeng, C. H., J. Dudhia, J. Klemp, and P. Sullivan (2007), Examining two-way grid nesting for large eddy simulation of the PBL using the WRF model, Monthly Weather Review, 135(6), 2295-2311, doi:10.1175/Mwr3406.1.

Moore, C. J. (1986), Frequency-response corrections for eddy-correlation systems, Boundary-Layer Meteorology, 37(1-2), 17-35, doi:10.1007/Bf00122754.

Oncley, S. P., et al. (2007), The Energy Balance Experiment EBEX-2000. Part I: Overview and energy balance, Boundary-Layer Meteorology, 123(1), 1-28, doi:10.1007/s10546-007-9161-1.

Panin, G. N., and C. Bernhofer (2008), Parametrization of turbulent fluxes over inhomogeneous landscapes, Izvestiya Atmospheric and Oceanic Physics, 44(6), 701-716, doi:10.1134/S0001433808060030.

Panin, G. N., G. Tetzlaff, and A. Raabe (1998), Inhomogeneity of the land surface and problems in the parameterization of surface fluxes in natural conditions, Theoretical and Applied Climatology, 60(1-4), 163-178, doi:10.1007/s007040050041.

Patton, E. G., P. P. Sullivan, and C.-H. Moeng (2005), The influence of idealized heterogeneity on wet and dry planetary boundary layers coupled to the land surface, Journal of the Atmospheric Sciences, 62(7), 2078-2097, doi:10.1175/jas3465.1.

Raasch, S., and G. Harbusch (2001), An analysis of secondary circulations and their effects caused by small-scale surface inhomogeneities using large-eddy simulation, Boundary-Layer Meteorology, 101(1), 31-59, doi:10.1023/A:1019297504109.

Schalkwijk, J., H. J. J. Jonker, and A. P. Siebesma (2016), An investigation of the eddy-covariance flux imbalance in a year-long large-eddy simulation of the weather at Cabauw, Boundary-Layer Meteorology, 160(1), 17-39, doi:10.1007/s10546-016-0138-9.

Steinfeld, G., M. O. Letzel, S. Raasch, M. Kanda, and A. Inagaki (2007), Spatial representativeness of single tower measurements and the imbalance problem with eddy-covariance fluxes: results of a large-eddy simulation study, Boundary-Layer Meteorology, 123(1), 77-98, doi:10.1007/s10546-006-9133-x.

Stoy, P. C., et al. (2013), A data-driven analysis of energy balance closure across FLUXNET research sites: The role of landscape scale heterogeneity, Agricultural and Forest Meteorology, 171, 137-152, doi:10.1016/j.agrformet.2012.11.004.

Stull, R. B. (1988), An Introduction to Boundary Layer Meteorology, Springer Science & Business Media, Dordrecht, Netherlands. 670 pp.

Talbot, C., E. Bou-Zeid, and J. Smith (2012), Nested mesoscale large-eddy simulations with WRF: performance in real test cases, Journal of Hydrometeorology, 13(5), 1421-1441, doi:10.1175/jhm-D-11-048.1.

Twine, T. E., W. Kustas, J. Norman, D. Cook, P. Houser, T. Meyers, J. Prueger, P. Starks, and M. Wesely (2000), Correcting eddy-covariance flux underestimates over a grassland, Agricultural and Forest Meteorology, 103(3), 279-300, doi:10.1016/S0168-1923(00)00123-4.

Wang, J. M., W. Z. Wang, S. M. Liu, M. G. Ma, and X. Li (2009), The Problems of Surface Energy Balance Closure: An Overview and Case Study, Advance in Earth Sciences, 24(7), 705-713, doi:10.11867/j.issn.1001-8166.2009.07.0705. (in Chinese)

Williams, M., et al. (2009), Improving land surface models with FLUXNET data, Biogeosciences, 6(7), 1341-1359, doi:10.5194/bg-6-1341-2009.

Wilson, K., et al. (2002), Energy balance closure at FLUXNET sites, Agricultural and Forest Meteorology, 113(1-4), 223-243, doi:10.1016/S0168-1923(02)00109-0.

Wohlfahrt, G., and P. Widmoser (2013), Can an energy balance model provide additional constraints on how to close the energy imbalance?, Agricultural and Forest Meteorology, 169, 85-91, doi:10.1016/j.agrformet.2012.10.006.

Wyngaard, J. C. (1985), Structure of the planetary boundary-layer and implications for its modeling, Journal of Climate and Applied Meteorology, 24(11), 1131-1142, doi:10.1175/1520-0450(1985)024<1131:Sotpbl>2.0.Co;2.

Xu, Z. W., Y. F. Ma, S. M. Liu, S. J. Shi, and J. M. Wang (2017), Assessment of the energy balance closure under advective conditions and its impact using remote sensing data, Journal of Applied Meteorology and Climatology, 56(1), 127-140, doi:10.1175/jamc-d-16-0096.1.

Zhou, Y., D. Li, H. Liu, and X. Li (2018), Diurnal variations of the flux imbalance over homogeneous and heterogeneous landscapes, Boundary-Layer Meteorology, 168(3), 417-442, doi:10.1007/s10546-018-0358-2.

Zhu, X., G. Ni, Z. Cong, T. Sun, and D. Li (2016), Impacts of surface heterogeneity on dry planetary boundary layers in an urban-rural setting, Journal of Geophysical Research: Atmospheres, 121(20), 12,164-112,179, doi:10.1002/2016JD024982.

Zuo, H., X. Xiao, Q. Yang, L. Dong, J. Chen, and S. Wang (2012), On the atmospheric movement and the imbalance of observed and calculated energy in the surface layer, Science China Earth Sciences, 55(9), 1518-1532, doi:10.1007/s11430-012-4378-3.